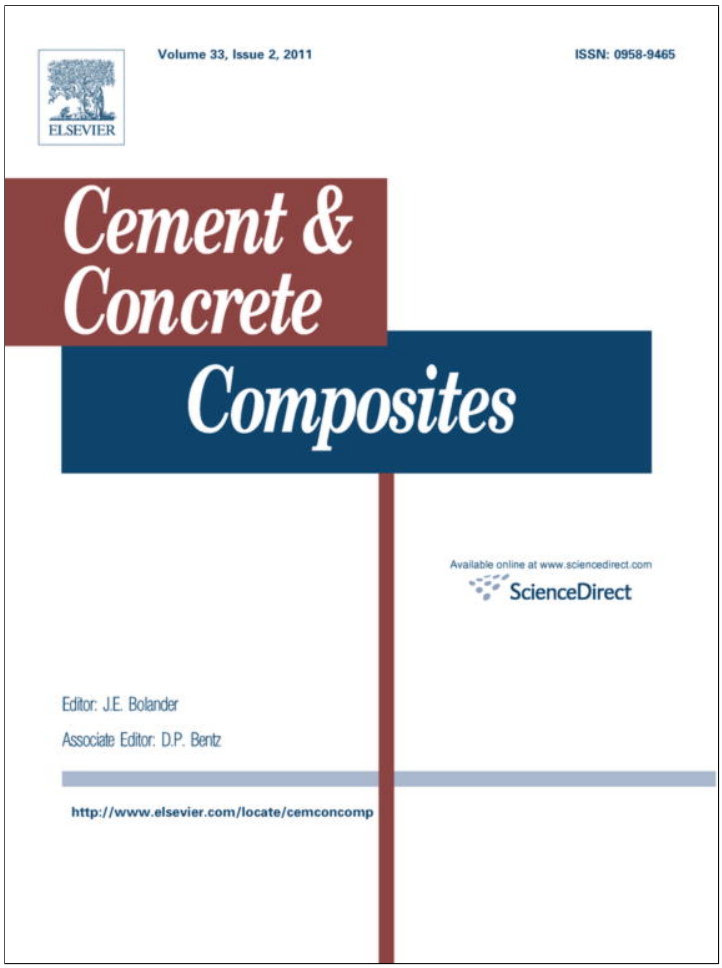

Cement & Concrete Composites 33 (2011) 163–170

Contents lists available at ScienceDirect

Cement & Concrete Composites

journal homepage: www.elsevier.com/locate/cemconcomp

Nanoindentation characteristics of alkali-activated aluminosilicate materials

Jiří Němeček *, Vít Šmilauer, Lubomír Kopecký

Department of Mechanics, Faculty of Civil Engineering, Czech Technical University in Prague, Thákurova 7, 166 29 Prague 6, Czech Republic

ARTICLE INFO

Article history:
Received 10 August 2009
Received in revised form 5 October 2010
Accepted 7 October 2010
Available online 15 October 2010

Keywords:
Nanoindentation
N-A-S-H gel
Geopolymer
Aluminosilicates
Fly ash
Metakaolin

ABSTRACT

Low calcium ground fly ash and metakaolin were activated with a sodium-silicate solution and cured under ambient and heat conditions. The resulting mature aluminosilicate composites were indented by several series of grids consisting of approximately 100 indents in each. The effective material volume affected by an indent was ≈1 μm^3. Statistical histogram plots of elastic properties of the main reaction product (N-A-S-H gel) as well as of other material phases were constructed. The deconvolution of histograms via four Gaussian distributions testified that the mature N-A-S-H gel has almost the constant intrinsic Young's modulus ≈17–18 GPa, irrespective of the curing procedure and activated material, i.e. fly ash or metakaolin.

1. Introduction

Alkali-activation of slag, metakaolin, fly ash and other aluminosilicate materials have been intensively investigated during the last decades; see [1–3] for comprehensive reviews. In comparison with conventional Portland cement-based composites these materials offer excellent durability in chemically aggressive environment [4], extended fire-resistance [3], lower basic creep [5], or environmental benefits [3]. On the other hand, they may suffer from efflorescense [6], high shrinkage under ambient curing [5,7], or from variations in chemical and physical properties at the level of activated aluminosilicate material [7].

In the past, various raw materials (slag, fly-ash, metakaolin, clay) were intermixed with strong alkaline solutions to synthesize a poorly crystallized inorganic gel binder [8]. Coined nomenclatures such as 'soil cement' [9], 'geopolymer' [10] or 'inorganic polymer' [2] have characterized more or less similar dissolution-precipitation processes taking place in a strong alkaline environment due to different starting materials. Here, the term N-A-S-H gel (aluminosilicate gel) will describe a binding matrix phase, embedding undissolved inclusions of remaining raw material.

In the past, alkali-activated materials were characterized by a variety of experimental techniques including FTIR, ESEM, MAS-NMR, XRD, DTA or calorimetry [8,11]. The majority of experimental data were linked directly to the atomic scale and nanostructure of N-A-S-H gel. However, all the above mentioned techniques suffer from data down-scaling by several orders of magnitude to the nanostructure of N-A-S-H gel. With this respect, nanoindentation sensing technique enables direct characterization of intrinsic mechanical properties on the micrometer and submicrometer resolution. The response is obtained directly from the close vicinity of a small indent without the interaction of distant material.

The objective of this paper aims at the quantification of intrinsic elastic properties of alkali-activated materials. A comprehensive study has never been performed in this field, although a few attempts can be found [12].

To shed light on different origins of N-A-S-H gel, both fly ash and metakaolin were activated under different curing temperatures. N-A-S-H gel appears as the main binding phase in both alkali-activated fly ash (AAFA) [13] and metakaolin (AAMK) [14], but mutual nanomechanical comparison has never been performed. The NMR and SEM analysis revealed that reaction products are structurally analogous in both materials [2]. Nanoindentation supports this hypothesis; intrinsic elastic properties of mature N-A-S-H gels were found to be independent of the curing temperature and activated materials as will be shown later in the paper.

2. Experimental part and evaluation methods

2.1. Materials, activation and curing of samples

Low calcium fly ash, class F, was obtained from the brown coal power plant Chvaletice, the Czech Republic. The Blaine specific surface was 210 m^2 kg^{-1}. The fly ash was ground in a small-scale ball mill to crush hollow cenospheres and to facilitate the reduction in

* Corresponding author. Tel.: +420 224 354 309.
E-mail addresses: jiri.nemecek@fsv.cvut.cz (J. Němeček), vit.smilauer@fsv.cvut.cz (V. Šmilauer), kopecky@fsv.cvut.cz (L. Kopecký).

0958-9465/$ - see front matter © 2010 Elsevier Ltd. All rights reserved.
doi:10.1016/j.cemconcomp.2010.10.005

Table 1
The chemical composition of ground fly ash and metakaolin (wt.%).

	SiO_2	Al_2O_3	Fe_2O_3	CaO	TiO_2	K_2O
Ground fly ash	51.9	32.8	6.3	2.7	1.89	2.12
Metakaolin	48.66	47.41	1.33	0.03	1.99	0.15

porosity. The XRD Rietveld analysis found the composition consisting of 70 vol.% amorphous phases, 24 vol.% mullite and 6 vol.% quartz.

Metakaolin originated from České lupkové závody a.s., Nové Strašecí, the Czech Republic. Chemical compositions of both materials are given in Table 1 and particle size distributions in Fig. 1.

The alkali-activator was previously optimized to yield a high compressive strength while maintaining workability [11]. The activator was prepared by dissolving NaOH pellets in tap water and adding sodium silicate (water glass). Table 2 summarizes the compositions of the mixtures. The final properties of the mixture can be controlled by three independent parameters (Table 2). Metakaolin requires significantly more activator due to its higher surface area.

Fly ash or metakaolin was intermixed with the activator for 5 min, cast in plastic ampoules 26 mm in diameter and 45 mm in height, gently vibrated for 5 min and sealed. Heat-cured fly ash or metakaolin samples were exposed to 80 °C for 12 h. Ambient-cured fly ash experienced a laboratory temperature ≈22 °C for the duration of six months prior to testing. Both materials are considered to be mature, although further polymerization and stiffening will continue forever. This is analogous to C-S-H aging known from the cement chemistry [15]. After a half-year from casting, the mean compressive strength of AAFA samples exceeds 70 MPa and that of AAMK 50 MPa, as determined on 100 mm cubes according to EN 12390.

2.2. Nanoindentation

Samples were cut to parallel slices of ≈10 mm in thickness, polished on fine emery papers and polishing cloth, and cleaned in an ultrasonic bath. Due to their varying heterogeneous composition, three representative areas were selected from each sample. Nanoindentation was carried out in a series of grids of 10 × 10 = 100 imprints in each area. The distance between individual indents varied in measurements in order to cover the heterogeneity of the sample. It was prescribed in the range of 10–50 μm. All together, around 700 imprints were carried out for each AAFA sample and around 500 imprints for AAMK sample.

Nanoindentation measurements were performed in a load control regime using the CSM Nanohardness tester equipped with a Berkovich tip. The trapezoidal loading diagram was prescribed for all tests (Fig. 2). Linear loading of 4 mN/min and lasting for 30 s produced a maximum load of 2 mN for all indents. The holding period (30 s) under the constant force followed, allowing material to creep. This stage is important for unbiasing the unloading stage [16]. The following unloading branch of 4 mN/min lasted for 30 s. The applied peak load of 2 mN led to maximum penetration depths ranging from 100 nm to 400 nm (average 260 nm) depending on the hardness of the indented material phase (Fig. 3). The effective depth captured by the tip of the nanoindenter can be roughly estimated as three to four times of the penetration depth for the Berkovich indentor [17]. It yields the effective depth of around 1 μm for this particular case.

Elastic properties were evaluated from nanoindentation tests according to the Oliver–Pharr methodology [18]. In this method, the unloading portion of the experimental load–penetration (P–h) curve is supposed to be elastic. Then, the analysis is based on an analytical solution known for rotational bodies punched into the elastic isotropic half-space. The indentation (reduced) modulus is then defined as follows:

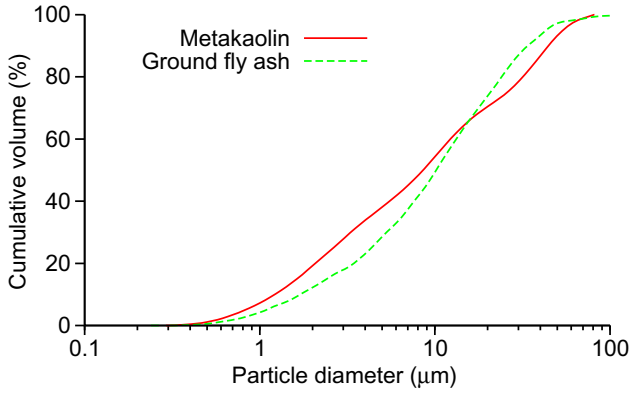

Fig. 1. Particle size distribution of ground fly ash and metakaolin.

Table 2
Mixture composition. Mass oxide ratii for activators and activator-to-solid mass ratii.

	Activator ratii		Activator to solid ratio (wt.%)
	Na_2O/SiO_2 (–)	H_2O/Na_2O (–)	
Ground fly ash	0.881	3.925	0.531
Metakaolin	1.669	2.743	1.416

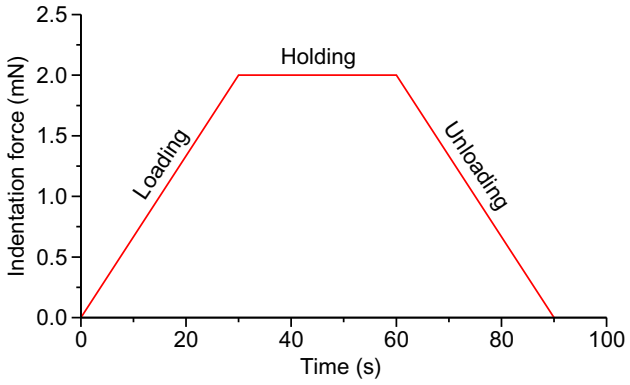

Fig. 2. Prescribed loading diagram in indentation experiments.

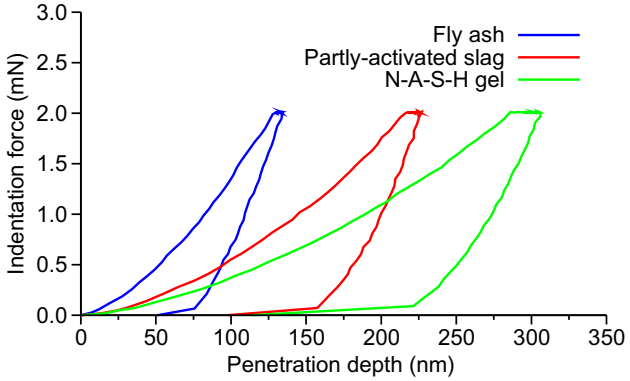

Fig. 3. Example of load-penetration curves obtained for distinct phases on AAFA samples by nanoindentation.

$$E_r = \frac{S\sqrt{\pi}}{2\beta\sqrt{A_c(h_{max})}} \quad (1)$$

where S is the contact stiffness evaluated as the initial slope of the unloading curve at the peak load and maximum depth h_{max}, i.e. $S = \frac{dP}{dh}|_{h=h_{max}}$, A_c is the projected contact area at the peak load, and β is the correction factor used for non-symmetrical indenters (1.034 for the Berkovich tip). The effect of non-rigid indenter can be accounted for by the following equation for the reduced modulus E_r:

$$\frac{1}{E_r} = \frac{1-\nu^2}{E} + \frac{1-\nu_i^2}{E_i} \quad (2)$$

where E and ν are the tested material elastic modulus and Poisson's ratio, respectively. E_i and ν_i are indenter's parameters (for diamond: $E_i = 1141$ GPa and $\nu_i = 0.07$). In our case, Poisson's ratio ν was assumed to be 0.2 for all measurements.

2.3. Deconvolution procedure

Individual AAFA and AAMK phase properties were determined by the statistical deconvolution applied to histograms of the E modulus. The deconvolution procedure was adopted from [17] but different minimizing criteria and a different generation of random sets of probability functions were used as will be demonstrated in the following.

Experimental histograms are constructed from all measurements whose number is N^{exp}, using equally spaced N^{bins} bins of the size b. Each bin is assigned with a frequency of occurrence f_i^{exp} that can be normalized with respect to the overall number of measurements as f_i^{exp}/N^{exp}. From that, we can compute the experimental probability density function (PDF) as a set of discrete values:

$$P_i^{exp} = \frac{f_i^{exp}}{N^{exp}} \cdot \frac{1}{b} \quad i = 1, \ldots, N^{bins} \quad (3)$$

The task of deconvolution into M phases represents finding $r = 1, \ldots, M$ individual PDFs related to single material phases. If we assume normal (Gauss) distributions, the PDF for a single phase can be written as:

$$p_r(x) = \frac{1}{\sqrt{2\pi s_r^2}} \exp \frac{-(x-\mu_r)^2}{2s_r^2} \quad (4)$$

in which μ_r and s_r are the mean value and standard deviation of the r-th phase computed from n_r values as:

$$\mu_r = \frac{1}{n_r}\sum_{k=1}^{n_r} x_k \quad s_r^2 = \frac{1}{n_r - 1}\sum_{k=1}^{n_r}(x_k - \mu_r)^2 \quad (5)$$

and x is the approximated quantity, i.e. the E modulus in our case. The overall PDF covering all M phases is then:

$$C(x) = \sum_{r=1}^{M} f_r p_r(x) \quad (6)$$

where f_r is the volume fraction of a single phase:

$$f_r = \frac{n_r}{N^{exp}} \quad (7)$$

Individual distributions can be found by minimizing the following error function:

$$\min \sum_{i=1}^{N^{bins}} \left[(P_i^{exp} - C(x_i))P_i^{exp}\right]^2 \quad (8)$$

in which we compute quadratic deviations between experimental and theoretical PDFs in a set of discrete points that is further weighted by the experimental probability in order to put emphasis on the measurements with a higher occurrence.

For our particular case, the bin size was chosen to be $b = 1$ GPa which provided sufficient resolution in all analyzed histograms. The number of mechanically distinct phases M was fixed in advance based on compositional analysis in ESEM and analysis of significant peaks in overall nanoindentation histograms. The M was set 4 for AAFA and 2 for AAMK samples, respectively. More specific arguments on the number of the phases M are given in the Section 3.

The minimization in Eq. (8) was based on the random Monte Carlo generation of M probability density functions satisfying the condition:

$$\sum_{r=1}^{M} f_r = 1 \quad (9)$$

In order to guarantee the convergence of the algorithm and to minimize the computational effort, the set of M PDFs in Eq. (4) was generated using the experimental dataset of all E moduli and separating it into M randomly spaced successive intervals. Mean values, standard deviations in Eq. (5) and volume fractions in Eq. (7) were computed in these intervals from corresponding E moduli and used in Eq. (6).

2.4. ESEM/EDX characterization

Samples from nanoindentation were repolished and scanned with secondary (SE) and backscattered electrons (BSE) in the electron microscope (Phillips XL30ESEM). The observations were complemented with the EDX microanalysis.

2.5. Porosity characterization

AAFA and AAMK samples were crushed to the size of a few millimeters, dried at 105 °C for 6 h and intruded by mercury (MIP, Autopore III Micromeritics) or measured by He-pycnometry (Micromeritics AccuPyc 1330). The combination of MIP and He pycnometry allows estimating the 'total' porosity from bulk and skeletal densities:

$$\varepsilon = \frac{\rho_{He}^{skeletal} - \rho_{Hg}^{bulk}}{\rho_{He}^{skeletal}}. \quad (10)$$

Both methods have their resolution limits; the size of a helium atom ($d \approx 0.062$ nm) from the bottom range and the limit of MIP from the top ($d \approx 120$ μm). Nevertheless, pore sizes of AAFA and AAMK samples fit well within both limits. The pore size distribution obtained from MIP is depicted in Fig. 4.

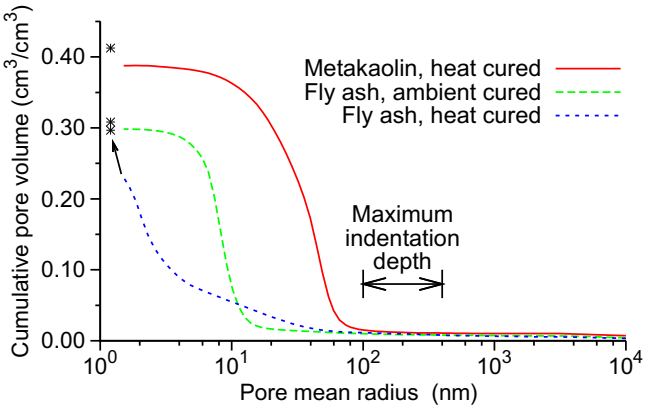

Fig. 4. Cummulative pore volume measured by MIP. Asterisk denotes total pore volume determined from Eq. (10).

3. Results and discussion

3.1. AAFA and AAMK porosity

Fig. 4 testifies that a different curing temperature changes the distribution of pores but preserves the total porosity in AAFA samples. These results seem to imply the same reaction stoichiometries, but with different reaction kinetics. Under an ambient curing temperature, AAFA remains in a quasi-liquid state for several days. During this period, N-A-S-H gel experiences slow polycondensation and syneresis with negligible mechanical restraint. Released water from polycondensation is expelled from the gel while forming larger pores [5,19]. From a series of observations, ambient-cured samples generally exhibit much larger autogeneous shrinkage as opposed to heat-cured specimens [5].

The indentation depth lies above the maximum pore size, Fig. 4. This is partially contradicted by ESEM images in Figs. 5, 10 which show porosity on a micrometer range. Such a discrepancy is explained as the bottle-neck effect which is controlled by fine-pore N-A-S-H gel. Careful avoidance of areas with large pores is a prerequisite for successful nanoindentation. Then, porosity occupies dominantly the scale below the indentation depth hence nanoindentation tests characterize mainly phases including their characteristic porosity from a lower scale. Especially for the AAMK, a part of porosity becomes comparable in size with the imprint which implies a slight reduction in an indentation moduli and an increase in the scatter. A series of nanoindentation tests (not shown here) performed with varying maximum depths ranging from 300 nm to 1500 nm showed that the mean modulus for N-A-S-H gel drops by ≈9% which is considered to be irrelevant.

3.2. ESEM and nanoindentation of heat-cured AAFA

Fig. 5 presents a characteristic structure of heat-cured AAFA formed from relicts of bullets of iron and/or iron oxides and compact Si–Al glass. It is estimated that roughly a half of fly ash was transformed to N-A-S-H gel [20].

Other ESEM observations led us to the conclusion that the AAFA heterogeneity occurs not only on a micrometer range but also on the scale of hundreds of μm, far exceeding the size of fly ash particles. This hypothesis was confirmed experimentally by nanoindentation. Three different representative regions were indented in three grids with different indent spacing. Fig. 6 shows that grids #1 and #2 lay in the areas rich in soft N-A-S-H gel while grid #3 hits the area of less activated fly ash with higher moduli.

Overall nanoindentation results from heat-cured AAFA samples (≈700 indents) are merged and plotted in Fig. 7. The histogram

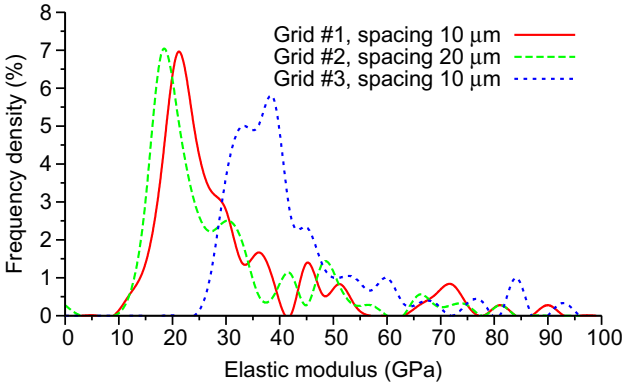

Fig. 6. Histogram of elastic moduli for three different indentation grids on a heat-cured AAFA sample.

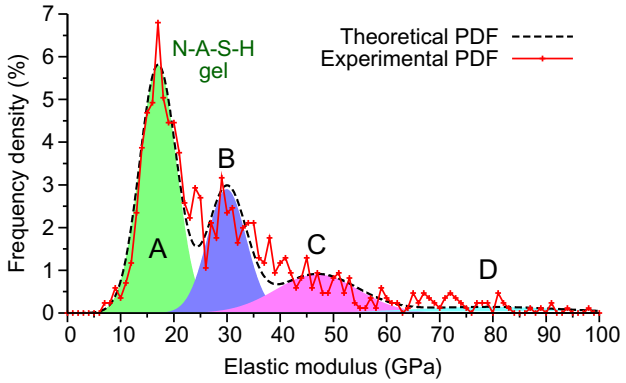

Fig. 7. Overall experimental and theoretical probability density functions with segmented four phases in heat-cured AAFA samples.

covers all phases, namely reaction products (N-A-S-H gel, partly-activated slags), including intrinsic porosity and unreacted fly ash (unreacted slags and glass particles). Based on thorough argumentation, four peaks in Fig. 7 were denoted and abbreviated as:

A. *N-A-S-H gel* – Pure N-A-S-H gel.
B. *Partly-activated slag* – N-A-S-H gel intermixed with slag-like particles.
C. *Nonactivated slag* – Porous nonactivated slag-like particles.
D. *Nonactivated compact glass* – Solid nonactivated glass spheres or their relicts after grinding.

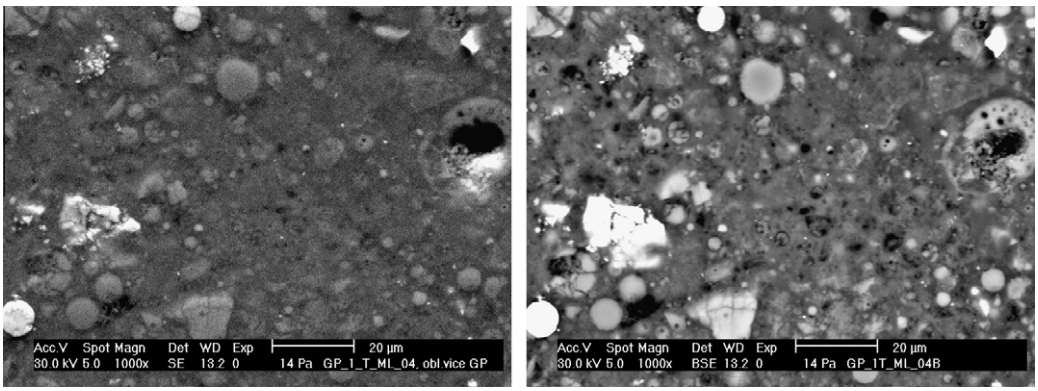

Fig. 5. AAFA heat-cured polished samples in SE (left) and BSE (right). In BSE image appear white iron and/or iron oxides bullets (intact), and compact Si–Al glass. The spotted light grey particles are the remnants of alkali-activated Si–Al–Na–K fly ash. The original slag particles were dissolved and transformed to dark grey compact matter of N-A-S-H gel. The black spots are capillary pores.

The alkaline activation of fly ash is essentially a selective process caused by a significant heterogeneity in the composition of raw fly ash [20]. The ability and kinetics of the reaction depends not only on the chemical and/or mineralogical composition of fly ash but predominantly also on the internal structure of the particle, and especially on the specific surface area. The observations show that preferential and rapid activation takes place in the slag-like, large size, Si–Al [Na, K, Mg, Fe, Mn] particles with a rich hollow structure on the micro level, and Fe–Mg [Si–Al] large slag particles [11]. The last two particles are easily dissolved and transformed to N-A-S-H gel.

The ESEM/EDX elementary simultaneous mapping in Fig. 8 does not provide a clue how to segment the indentation histogram into four phases, Fig. 7. Except for iron and calcium, the spatial distributions of measured elements are very homogeneous.

In order to support the proposed phase assignment, nanoindentation focused on partly-activated slag and compact glass particle. Indents were located in a row coming from the outbound particle rim towards the unreacted core as shown in Fig. 9. The resulting elastic modulus is increasing as approaching towards the compact unreacted core. The outward particle rim has a stiffness corresponding to the N-A-S-H gel in the reacted matrix (≈17–18 GPa) whereas the hard particle core is bounded by a zone with approximately doubled stiffness. This finding led us to the conclusion that indentation hits all four segmented phases.

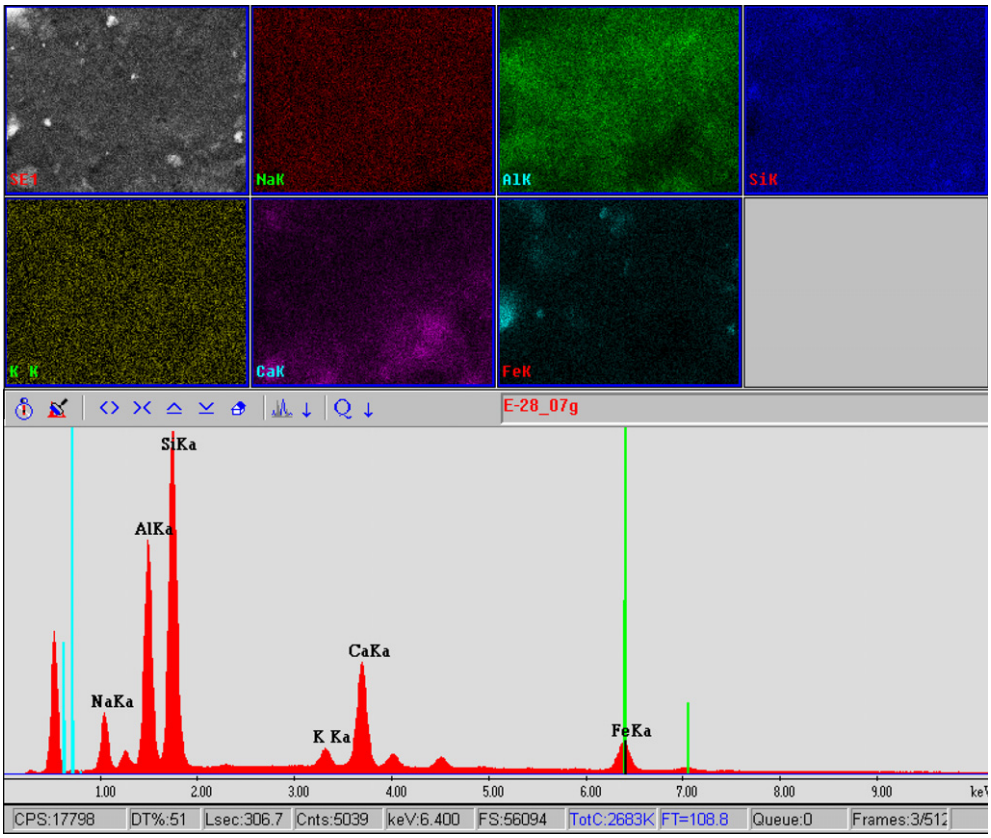

Fig. 8. Multiple elementary EDX mapping of the polished section of heat-cured AAFA taken for six elements (Na, Al, Si, K, Ca and Fe).

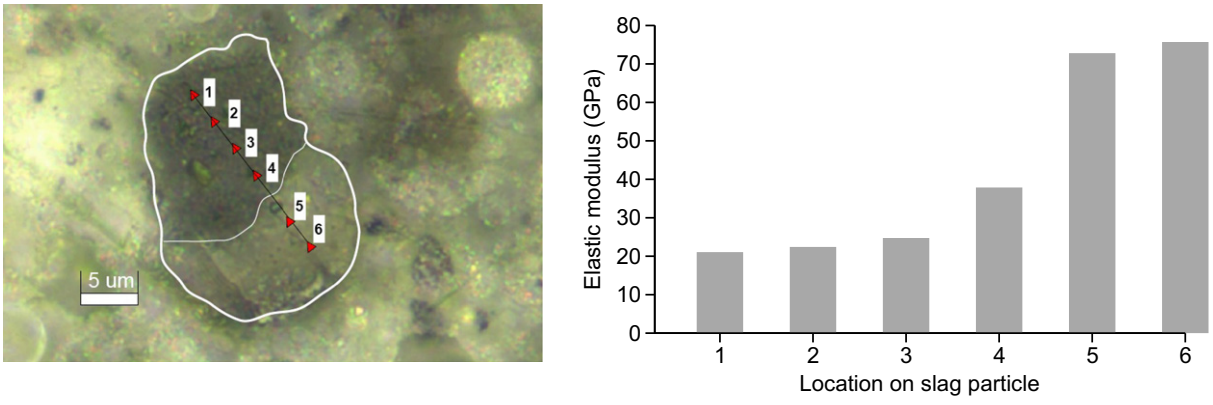

Fig. 9. Partly-activated slag particle in the heat-cured AAFA sample with marked locations of indents (left) and measured moduli (right).

3.3. ESEM and nanoindentation of ambient-cured AAFA

Fig. 10 shows a typical morphology for ambient-cured AAFA. The comparison with heat-cured AAFA in Fig. 5 shows more capillary pores and darker N-A-S-H gel. This supports the ongoing slow process of N-A-S-H gel syneresis.

Ambient curing produces more homogeneous AAFA on the scale of hundreds of micrometers. In this particular case, three grids from different locations give mutually comparable results, Fig. 11.

When compared to heat-cured AAFA, ambient-cured specimens have a much smaller peak associated with partly-activated slag. Such a result points to the higher extent of an activation under low temperatures. Also, the third and fourth peaks of nonactivated particles are smaller (Fig. 12).

3.4. ESEM and nanoindentation of heat-cured AAMK

The microstructure of heat-cured metakaolin is very homogeneous (Fig. 13). The reason lies in a very monotonous chemical and mineralogical composition of a metakaoline precursor. The dissolving process of the metakaoline matrix is homogeneous and the majority of metakaolin reacts under a strong alkaline activator [21].

Nanoindentation was again performed as a series of five grids of 100 indents each with mutual distances of 10–20 μm (Fig. 14). It follows that, from the micromechanical perspective, activated metakaolin is homogeneous, i.e. raw nonactivated metakaolin is embedded in N-A-S-H gel under the resolution of indentation (≈1 μm). Raw metakaolin is present in the quantity of less than 11.2% by mass. This statement is based on the HCl attacked samples with a weaker 12 M NaOH activator [21].

Statistical deconvolution testifies that N-A-S-H gel is the only dominant phase as can be seen in Fig. 15. Therefore, the number of mechanically distinct phases *M* was set to 2 in the deconvolution algorithm. The mean value of the dominant phase (17.72 GPa) well corresponds to the N-A-S-H gel from heat- and ambient-cured AAFA samples.

3.5. Summarized result for AAFA and AAMK samples and comparison with similar materials

Table 3 summarizes the results from nanoindentation deconvoluted into distinct phases and showing their intrinsic *E* moduli and frequencies of occurrence. As obvious, N-A-S-H gel was identified with a very similar intrinsic modulus (≈17–18 GPa) regardless of the precursor material. It is worthy to mention that the

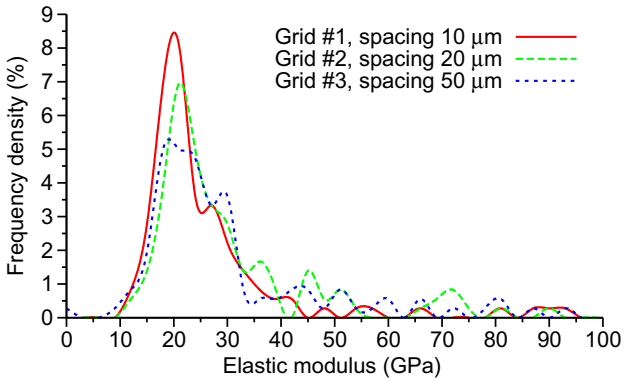

Fig. 11. Histogram of elastic moduli for three different indentation grids on an ambient-cured AAFA sample.

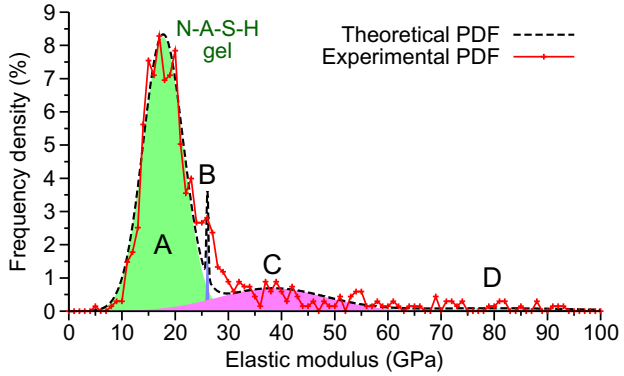

Fig. 12. Overall experimental and theoretical probability density functions with segmented four phases in ambient-cured AAFA samples.

elastic modulus of N-A-S-H gel is similar to low-density C-S-H gel formed in cement paste (17.8 ± 4.2 GPa, [22]). Composite materials such as concrete will yield very similar elasticity when cement binder is replaced with AAFA or AAMK. Another material, fused silica, has a typical modulus 72 ± 2 GPa and this value roughly corresponds to compact glass found in fly ash. Mullite (aluminosilicate mineral consisting of 72% Al_2O_3 and 28% SiO_2), that is partly present in the raw AAFA material, has $E = 223.8 \pm 4.65$ GPa, [23]. Such a high value of the *E* modulus

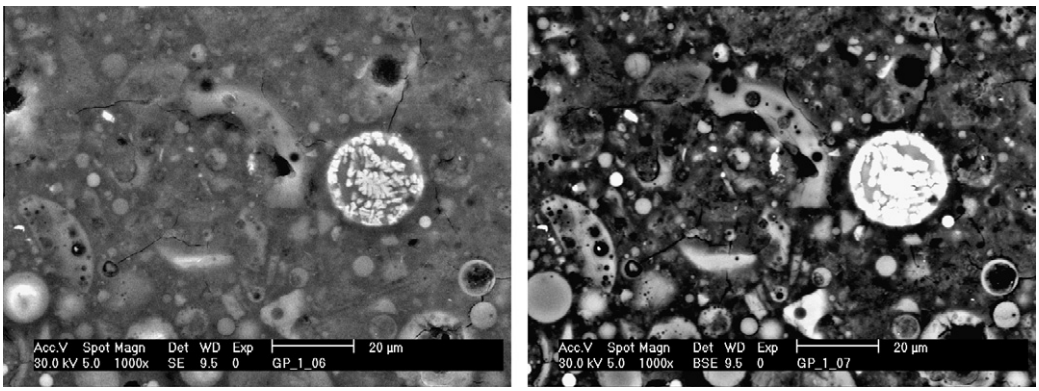

Fig. 10. AAFA ambient-cured polished samples in SE (left) and BSE (right). BSE image shows white iron and/or iron oxides bullets (intact), and compact Si–Al glass. The spotted light grey particles are partly alkali-activated Si–Al–Na–K fly ash. The original slag particles are dissolved and transformed to dark grey compact matter of N-A-S-H gel. The black spots are capillary pores.

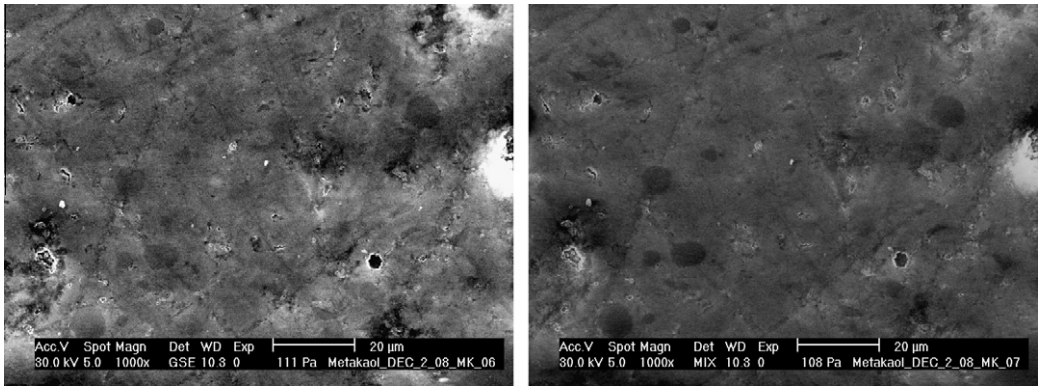

Fig. 13. AAMK heat-cured polished samples in SE (left) and BSE (right). A few microcracks and pores are distinguishable.

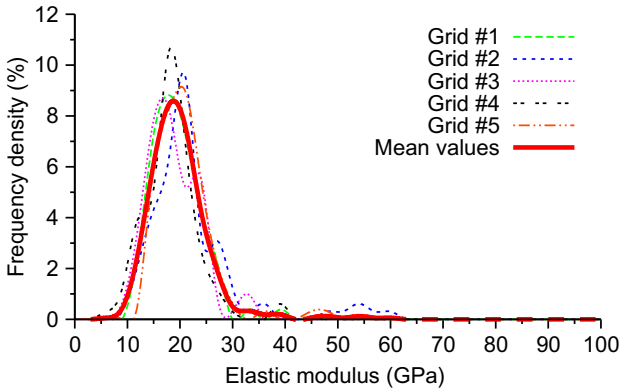

Fig. 14. Histogram of elastic moduli for five different indentation grids on a heat-cured AAMK sample.

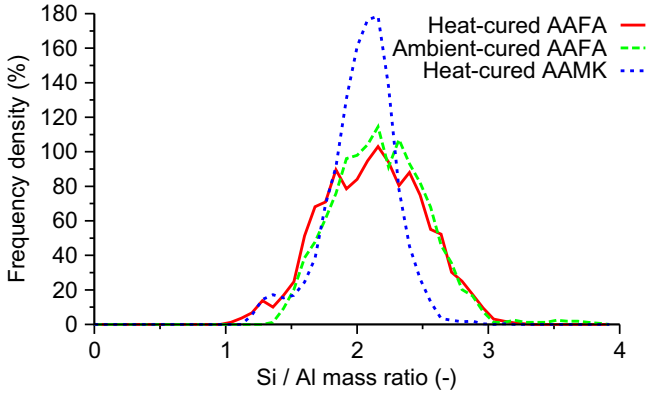

Fig. 16. Histograms of EDX line analyses demonstrating similar Si–Al distribution in studied three activated materials.

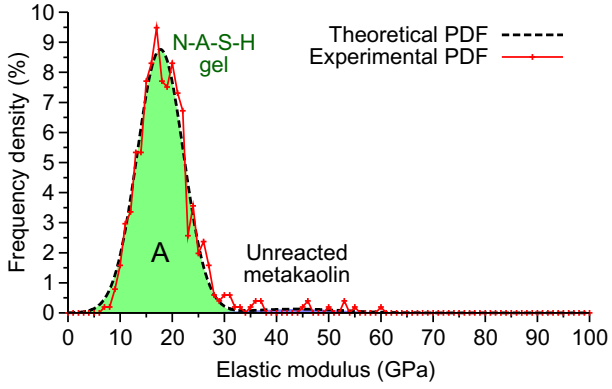

Fig. 15. Overall experimental and theoretical probability density functions with a segmented dominant N-A-S-H gel phase and unreacted metakaolin in an AAMK sample.

has never been observed in measurements, either on AAFA or AAMK samples. From nanoindentation virtually no values higher than ≈100 GPa were obtained. The reason lies in compliant surrounding matrix which does not allow measuring the intrinsic properties of such hard particles. True intrinsic values obtained by nanoindentation can be achieved if the stiffness contrast between matrix and inclusion is less than five [17,24].

The indispensable role of nanoindentation in assessing intrinsic elastic properties is again demonstrated in Fig. 16 from a chemical perspective. The histograms in Fig. 16 were obtained by the EDX line analyses, performed on all three activated materials, in the amount 2000 points each. The heat-cured AAMK could be deconvoluted into metakaolin remnants and N-A-S-H gel with Si–Al mean mass ratio 2.16. While alkali-activated materials exhibit very similar Si–Al distribution in Fig. 16, the oxide arrangement leads to tremendously different elastic behavior as already demonstrated in Figs. 7, 12, and 15.

Table 3
Elastic moduli (GPa) of individual material phases in heat- and ambient-cured AAFA and heat-cured AAMK. The values in parentheses denote frequency.

Phase/precursor and curing	AAFA		AAMK
	Heat-cured	Ambient-cured	Heat-cured
A. N-A-S-H gel	17.03 ± 3.48 (50.7%)	17.72 ± 3.75 (77.5%)	17.72 ± 4.43 (97.2%)
B. Partly-activated slag	29.95 ± 3.66 (26.6%)	26.06 ± 0.18 (1.1%)	
C. Nonactivated slag	46.90 ± 7.76 (17.6%)	38.27 ± 10.13 (17.5%)	
D. Nonactivated compact glass	79.15 ± 14.34 (5.1%)	79.65 ± 16.99 (3.9%)	
Unreacted metakaolin			43.91 ± 8.69 (2.8%)

4. Conclusions

The extensive nanoindentation testing and ESEM analysis of alkali-activated fly ash and metakaolin samples led to the conclusions:

1. The intrinsic E modulus of the main reaction product, the N-A-S-H gel, lies in the range of 17–18 GPa and seems to be independent of the precursor material (fly-ash or metakaolin) and the temperature curing regime (ambient or heat cured) for a given mixture composition. Such a modulus is very close to a typical value of low-density C-S-H gel, 17.8 GPa, found in cement paste [22]. From an elastic perspective, potential coexistence of C-S-H and N-A-S-H gels is excellent [13].
2. Further deconvolution of indentation histograms identified other elastically distinct phases. Based on thorough argumentation and SEM images, three other morphologically distinct phases were found in AAFA and one in AAMK. The same finding was found on the indenting slag-like activated porous particle.
3. Statistical EDX line analysis provided no evident correlation between chemical composition and the E modulus. Found mean Si–Al mass ratio of N-A-S-H gel is 2.16, corresponding exactly to the value for mature N-A-S-H gel in the form of probably zeolite crystals [8].
4. The slow process of ambient-curing produces a more homogeneous microstructure where no heterogeneity appears on the scale above $10 \times 50 \approx 500$ μm as evident from Fig. 11. In contrast, three indentation grids of heat-cured AAFA in Fig. 6 show the significant heterogeneity occuring above the scale $10 \times 10 \approx 100$ μm. This emphasizes the ion transport and equilibration of the oligomer concentration during the activation process.
5. Although the study covered typical and mature alkali-activated materials, it is not meant to be exhaustive. Several issues and their effect on elasticity remained open, especially the composition of the mixture and the activator, early age, aging, or ongoing N-A-S-H syneresis.
6. Understanding intrinsic constituent properties in a complex material allows addressing and modeling distinct mechanisms on multiscales in terms of material evolution, performance, optimization and durability. Over history, upscaling of elasticity [25,26], viscoelasticity [27], or shrinkage [28] has proven to be a simple, yet powerful method of conjunction between micromechanics and material engineering.

Acknowledgements

This study was part of the research project Czech Science Foundation Grant 103/08/1639 "Microstructure of inorganic alumosilicate polymers" and Czech Science Foundation Grant 103/09/1748 "Integration of experimental nanoindentation with numerical tools for upscaling of nanomechanical properties of heterogeneous materials". Their support is gratefully acknowledged.

References

[1] Pacheco-Torgal F, Castro-Gomes J, Jalali S. Alkali-activated binders: a review: part 1. Historical background, terminology, reaction mechanisms and hydration products. Construct Build Mater 2008;22(7):1305–14.
[2] Duxson P, Fernández-Jiménez A, Provis JL, Lukey GC, Palomo A, van Deventer JSJ. Geopolymer technology: the current state of the art. J Mater Sci 2007;42(9):2917–33.
[3] Provis JL, van Deventer JSJ, editors. Geopolymers: structures, processing, properties and industrial applications. 1st ed., Woodhead Publishing Ltd.; 2009.
[4] Fernandez-Jimenez A, García-Lodeiro I, Palomo A. Durability of alkali-activated fly ash cementitious materials. J Mater Sci 2007;42:3055–65. doi:10.1007/s10853-006-0584-8.
[5] Wallah SE, Rangan BV. Low-calcium fly ash-based geopolymer concrete: long term properties. Research report GC 2, Curtin University of Technology, Perth, Australia; 2006.
[6] Škvára F, Kopecký L, Myšková L, Šmilauer V, Alberovská L, Vinšová L. Aluminosilicate polymers – influence of elevated temperatures, efflorescence. Ceramics – Silikáty 2009;53(4):276–82.
[7] Shi C, Krivenko PV, Roy D. Alkali-activated cements and concrete. Taylor & Francis; 2006.
[8] Fernández-Jiménez A, Palomo A. Composition and microstructure of alkali activated fly ash binder: effect of the activator. Cem Concr Res 2005;35:1984–92.
[9] Glukhovsky VD. Soil silicates (Gruntosilikaty), Kiev. USSR: Budivelnik Publisher; 1959.
[10] Davidovits J. Synthesis of new high-temperature geo-polymers for reinforced plastics/composites. In: Proceedings of PACTEC'79, society of plastic engineers; 1979. p. 151–4.
[11] Škvára F, Kopecký L, Šmilauer V, Bittnar Z. Material and structural characterization of alkali activated low-calcium brown coal fly ash. J Hazard Mater 2009;168:711–20.
[12] Beleña I, Zhu W. Nanoindentation study of Na-geopolymers exposed to high temperatures. In: Bittnar Z, Bartos P, Zeman J, Němeček J, Šmilauer V, editors. Proceedings of the nanotechnology in construction, vol. 3. Springer; 2009. p. 169–74.
[13] Palomo A, Fernández-Jiménez A, Kovalchuk G, Ordoñez LM, Naranjo MC. Opc-fly ash cementitious systems: study of gel binders produced during alkaline hydration. J Mater Sci 2007;42(9):2958–66.
[14] Granizo ML, Blanco-Varela MT, Martínez-Ramírez S. Alkali activation of metakaolins: parameters affecting mechanical, structural and microstructural properties. J Mater Sci 2007;42(9):2934–43.
[15] Lea F. Lea's chemistry of cement and concrete. 4th ed. Elsevier; 2004.
[16] Němeček J. Creep effects in nanoindentation of hydrated phases of cement pastes. Mater Character 2009;60(9):1028–34. doi:10.1016/j.matchar.2009.04.008.
[17] Constantinides G, Chandran KSR, Ulm F-J, Vliet KJV. Grid indentation analysis of composite microstructure and mechanics: principles and validation. Mater Sci Eng A 2006(430):189–202.
[18] Oliver WC, Pharr GMR. An improved technique for determining hardness and elastic modulus using load and displacement sensing indentation experiments. J Mater Res 1992;7:1564–83.
[19] Hardjito D, Rangan BV. Development and properties of low-calcium fly ash-based geopolymer concrete. Research report GC 1, Curtin University of Technology, Perth, Australia, Faculty of Engineering; 2005.
[20] Fernández-Jiménez A, Palomo A, Criado M. Microstructure development of alkali-activated fly ash cement: a descriptive model. Cem Concr Res 2004;35:1204–9.
[21] Granizo ML, Alonso S, Blanco-Varela MT, Palomo A. Alkaline activation of metakaolin: effect of calcium hydroxide in the products of reaction. J Am Ceram Soc 2002;85(1):225–31.
[22] Constantinides G, Ulm F-J. The effect of two types of C–S–H on the elasticity of cement-based materials: results from nanoindentation and micromechanical modeling. Cem Concr Res 2004;34(1):67–80.
[23] Nath S, Dey A, Mukhopadhyay AK, Basu B. Nanoindentation response of novel hydroxyapatite-mullite composites. Mater Sci Eng A 2009(513–514):197–201.
[24] Němeček J, Lukeš J. On the evaluation of elastic properties from nanoindentation of heterogeneous systems. Chemické Listy 2010;104(15):s279–82.
[25] Bernard O, Ulm F-J, Lemarchand E. A multiscale micromechanics-hydration model for the early-age elastic properties of cement-based materials. Cem Concr Res 2003;33(9):1293–309.
[26] Šmilauer V, Bittnar Z. Microstructure-based micromechanical prediction of elastic properties in hydrating cement paste. Cem Concr Res 2006;36(9):1708–18.
[27] Pichler C, Lackner R. A multiscale creep model as basis for simulation of early-age concrete behavior. Comput Concr 2008;5(4):295–328.
[28] Pichler C, Lackner R, Mang HA. A multiscale micromechanics model for the autogenous-shrinkage deformation of early-age cement-based materials. Eng Fract Mech 2007;74:34–58.